Experimental Decomposition of the Positive Bias Temperature Stress-induced Instability in Self-aligned Coplanar InGaZnO Thin-film Transistors and its Modeling based on the Multiple Stretched-exponential Functions

Dae Hwan Kim,[1, a] Sungju Choi,[1] Juntae Jang,[1] Hara Kang,[1] Dong Myong Kim,[1] Sung-Jin Choi,[1] Yong-Sung Kim,[2] Saeroonter Oh,[3] Ju Heyuck Baeck,[4] Jong Uk Bae,[4] Kwon-Shik Park,[4] Soo Young Yoon,[4] and In Byeong Kang [4]

[1]School of Electrical Engineering, Kookmin University, Seoul 02707, Korea
TEL: +82-2-910-4872, FAX : +82-2-910-4449, [a]Contact Author E-mail: drlife@kookmin.ac.kr
[2]Korea Research Institute of Standards and Science, Daejeon 34113, Korea
[3]Division of Electrical Engineering, Hanyang University, Ansan, Gyeonggi-do, 15588, Korea
[4]Research and Development Center, LG Display Co., Paju, Gyeonggi-do, 413-811, Korea

Abstract

Decomposition of the positive gate-bias temperature stress (PBTS)-induced instability into contributions of distinct mechanisms is experimentally demonstrated in top-gate self-aligned coplanar amorphous InGaZnO thin-film transistors and validated by reproducing the PBTS time-evolution of I-V characteristics through the TCAD simulation into which the extracted density-of-states and charge trapping are incorporated.

Author Keywords

amorphous InGaZnO thin-film transistors; top-gate self-aligned coplanar structure; experimental decomposition of positive-bias temperature stress instability.

1. Introduction

Although amorphous InGaZnO (a-IGZO) thin-film transistors (TFTs) have been successfully employed in commercial display products, such as organic light-emitting diode (OLED) displays and liquid-crystal displays (LCDs),[1-4] the device stability requirement ironically becomes more stringent in future displays with higher resolution, higher frame rate, higher brightness, and longer product lifetime. Current-driving TFTs in an OLED pixel, as well as TFTs in gate-driver circuitry are often under the influence of positive gate-bias temperature stress (PBTS). Under the influence of PBTS, the threshold voltage (V_T) shifts in the positive direction. The physical origin of PBTS instability has been classified largely by either 1) trapping of electrons in the gate insulator (GI),[5,6] or 2) change in defect states in the active region.[7-9]

Generally, in previous reports, the PBTS instability has been attributed to one of the two stated mechanisms as the dominant mechanism. For example, when the transfer curves show a parallel shift and the subthreshold swing (SS) does not change with stress time, charge trapping is referred to as the dominant mechanism. However, this method is not always applicable, since it is hard to determine how much of each degradation mechanism can be attributed to the V_T shift (ΔV_T) when the SS does change. If the newly created defects in the channel in the vicinity of the active-to-GI interface have an energy well below the Fermi-level, it might not show up as an increase in SS value.[10] Moreover, the dominant mechanism is dependent on the device structure, fabrication process, and stress conditions. Since several degradation mechanisms of different nature may take part in the PBTS instability, ascribing to one particular dominant mechanism may be irrelevant. Therefore, a novel method that can systematically determine the quantitative contribution of several mechanisms is required. On the other hand, the a-IGZO TFTs with top-gate self-aligned (TG-SA) coplanar structure were successfully implemented in manufacturing the UHD OLED televisions.[4] The TG-SA coplanar structure [Fig. 1(a)] has many advantages, such as higher performance due to no overlap capacitance between gate and source/drain (S/D), better channel length scalability, better process controllability through subsequent processes including GI deposition, plasma treatment, and thermal annealing, and a lower V_T with better SS due to its better electrostatic integrity than bottom-gate (BG) structure.[11,12] However, the instability of TG-SA coplanar IGZO TFTs has been rarely investigated in spite of its great importance.[6,12]

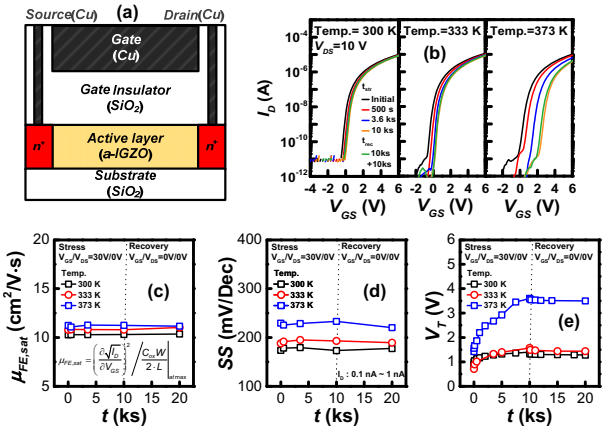

Figure 1. (a) Device structure of TG SA coplanar a-IGZO TFT. The PBTS time-evolutions of (b) transfer curves, (c) $\mu_{FE,sat}$, (d) SS, and (e) V_T during PBTS ($t_{str}=10^4$ s) and additional 10^4 s recovery time ($t_{rec}=2\times10^4$ s).

Motivated by these backgrounds, we proposed the subgap density-of-states (DOS) based systematic decomposition of the positive bias stress-induced ΔV_T in TG-SA coplanar a-IGZO TFTs and demonstrated it at a room temperature.[13] In this work, as a further study for our previous work, the decomposition of PBTS instability into contributions of distinct mechanisms is experimentally demonstrated at several temperatures in TG-SA coplanar a-IGZO TFTs and further validated with the activation energy for an individual mechanism by reproducing the PBTS time-evolution of I-V characteristics through the TCAD simulation into which the extracted DOS and charge trapping are incorporated. It is also found that the quantitative

 ISSN 0097-996X/17/4701-0298-$1.00

decomposition of PBTS ΔV_T accompanied with the multiple stretched-exponential (MSE) model enables an effective assessment of the complex degradation nature of multiple PBTS physical processes occurring simultaneously.

2. Fabrication Process & Device Characteristics

The a-IGZO TFTs have a TG-SA coplanar structure, as shown in Fig. 1(a). The 30-nm-thick a-IGZO layer (In:Ga:Zn=1:1:1 at%) is deposited by dc sputtering. A 100-nm SiO_2 layer is deposited by PECVD to serve as the GI. Interlayer dielectrics are deposited and patterned for S/D openings. Gate and S/D electrodes are formed by sputtering Cu/MoTi. Device size is W/L=12/6 μm. Figures 1(b)~(e) show the measured PBTS time-evolutions of transfer curves, field-effect mobility ($\mu_{FE,sat}$), SS, and V_T during PBTS ($t_{str}=10^4$ s, V_{GS}=30 V, and V_{DS}=0 V) and additional 10^4 s recovery time ($t_{rec}=2\times10^4$ s, $V_{GS}=V_{DS}$=0 V).

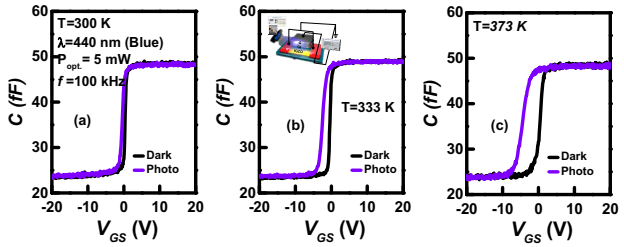

Figure 2. Photo-response of C-V curve at (a) 300 K, (b) 333 K, and (c) 373 K. Inset in (b) shows the schematic of measurement setup.

Subgap DOS of a-IGZO is extracted from the photo-response of C-V curves [Fig. 2].[14] The measured bandgap of IGZO is E_g=3.03 eV while the energy of incident photons is 2.82 eV. Extracted DOS's are shown in the symbols in Figures 3(a)~(d), which consist of four components according to their distribution shapes in energy level: donor-like tail states (g_{TD}), excess oxygen defect states (g_{Oex}), acceptor-like deep states (g_{DA}) and tail states (g_{TA}), in increasing order of the energy levels. The DOS profile is found to be well fitted with following model equations [lines in Figures 3(a)~(d)] as:

$$g_{TD}(E)+g_{Oex}(E)=N_{TD}\exp\left(-\frac{E-E_V}{kT_{TD}}\right)+N_{Oex}\exp\left(-\left(\frac{E-E_V-E_{Oex}}{kT_{Oex}}\right)^2\right) \quad (1)$$

$$g_{TA}(E)+g_{DA}(E)=N_{TA}\exp\left(-\frac{E_C-E}{kT_{TA}}\right)+N_{DA}\exp\left(-\left(\frac{E_C-E_{DA}-E}{kT_{DA}}\right)^2\right) \quad (2)$$

The DOS parameters are summarized in Table I. Here, the N_{DOS}, such as N_{TD}, N_{Oex}, N_{DA} and N_{TA}, is the density and the kT_{DOS}, such as kT_{TD}, kT_{Oex}, kT_{DA} and kT_{TA}, is the characteristic energy, respectively. The E_{DOS}, such as E_{Oex} and E_{DA}, is the center energy of the Gaussian DOS peak. The E_C/E_V is the conduction/valence band edge.

The only component that gives a significant change in DOS during PBTS is the g_{Oex}, which is located in the energy range of 0.7 eV above E_V, as shown in Figures 3(a)~(d) and Table I. This g_{Oex} seems to partially relate with the ppπ* (occupied) states in the O_{ex} (excess oxygen) peroxide (i.e., O-O dimer) configuration, and also with the ppσ* states after electron-capture by the peroxide.[15,16] During PBTS, the empty ppσ* anti-bonding state in the conduction bands captures two electrons letting the peroxide transform into the fully-oxidized state, i.e., $(O\text{-}O_{ex})^{2-}+2e^-\rightarrow O^{2-}+O^{2-}$, as seen in Fig. 3(e).[15] The occupied ppσ* state then moves into the g_{Oex} energy range as illustrated in Fig. 3(f).[16] Thus, the actual change of the g_{Oex} originates from the increase of the ppσ* state capturing electrons, and that is the reason why g_{Oex} has an acceptor-like character. The increase of g_{Oex} should accompany the decrease of empty ppσ* states inside the conduction bands.

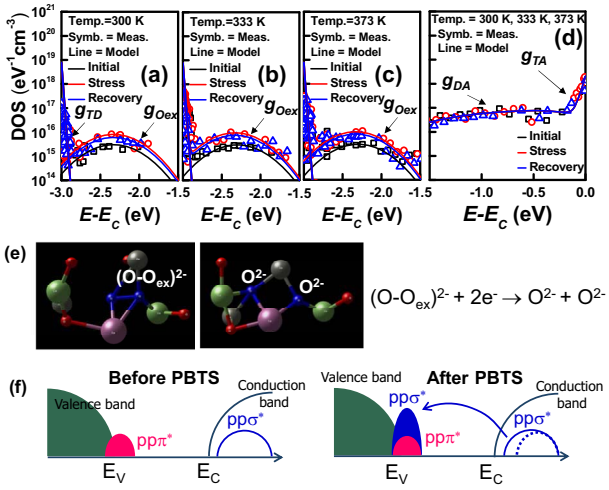

Figure 3. Extracted DOS near (a)-(c) E_V and (d) E_C during PBTS at various temperatures. Experiments and models are denoted as open symbols and lines. Schematic views illustrating (e) the microscopic origin of $\Delta V_{T,DOS}$ and (f) the increase of g_{Oex} during PBTS.

Table 1. Extracted DOS parameters during PBTS

Parameter			N_{DOS} [$eV^{-1}cm^{-3}$]	kT_{DOS} [eV]	E_{DOS} [eV]
g_{TA} (Acceptor-like tail states)			2.0×10^{18}	0.03	-
g_{DA} (Acceptor-like deep states)			6.0×10^{16}	0.75	0.8
g_{Oex}	T= 300 K	Initial	0.3×10^{16}	0.4	0.7
		After stress	0.8×10^{16}		
		After recovery	0.65×10^{16}		
	T= 333 K	Initial	0.3×10^{16}		
		After stress	0.95×10^{16}		
		After recovery	0.75×10^{16}		
	T= 373 K	Initial	0.3×10^{16}		
		After stress	1.1×10^{16}		
		After recovery	0.8×10^{16}		
g_{TD} (Donor-like tail states)			5.0×10^{18}	0.015	-

3. Experimental Decomposition of PBTS ΔV_T

Figure 4 illustrates the decomposition scheme of a total ΔV_T, i.e., $\Delta V_{T,tot}(t)$, into the contributions of distinct mechanisms. The measured $\Delta V_{T,tot}(t)$ at a specific t_{str} is schematically illustrated in Fig. 4(a). In the recovery characteristics, the ΔV_T lowers quickly at the early stage of recovery, and saturates to a certain value. The t_{rec} is defined as the time when $d\Delta V_{T,tot}(t)/dt < 10^{-6}$ (V/s). The saturated value of the recovery portion ($\Delta V_{T,fast}$) is measured after t_{rec} as denoted by ② in Fig. 4(a). This fast recovery component may still include several mechanisms and requires further decomposition.

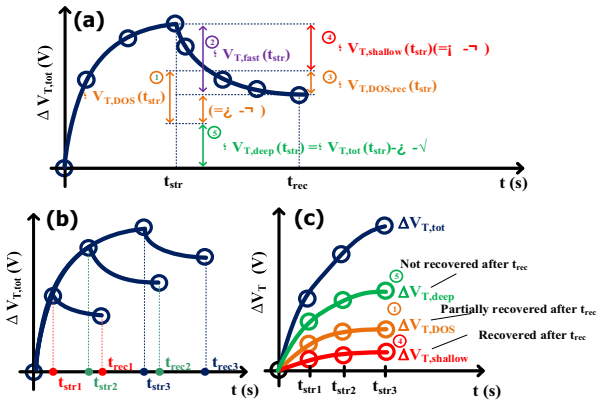

Figure 4. (a) The procedure of experimental decomposition of PBTS $\Delta V_{T,tot}$ at specific t_{str} and t_{rec}. The circled number indicates the order of acquiring experimental data. (b) The stress-time-divided measurement and (c) finally decomposed ΔV_T as the function of t_{str}.

First, we investigate ΔV_T recovery characteristics not only after the entire stress stage (t_{str} in Fig. 4(a)), but also in between stress-time intervals during the stress stage as denoted by t_{str1}, t_{str2}, and t_{str3} in Fig. 4(b). In this way, $\Delta V_{T,fast}$ is sampled at $t=t_{str1}$, t_{str2}, and t_{str3} in order to trace the PBTS time-evolution of $\Delta V_{T,fast}$ during $t=t_{str}$, which is called as "the stress-time-divided measurement". Second, we measure the ΔV_T contribution caused by the PBTS-induced change in DOS of the channel layer, i.e., $\Delta V_{T,DOS}$ which is denoted by ① in Fig. 4(a), and trace the PBTS time-evolution of $\Delta V_{T,DOS}$ as denoted by t_{str1}, t_{str2}, and t_{str3} in Fig. 4(b) and Table I. Then, we express the positive ΔV_T due to the increase of g_{Oex} after the PBTS during t_{str} as:

$$\Delta V_{T,DOS}(t_{str}) = \frac{qt_{IGZO}}{C_{ox}}\left(\int_{E_V}^{E_F} g_{Oex}(E,\ t=t_{str})\,dE - \int_{E_V}^{E_F} g_{Oex}(E,\ t=0)\,dE\right) \quad (3)$$

where q is the elementary charge of an electron, t_{IGZO} is the active layer thickness, and C_{ox} is the gate insulator capacitance per unit area. We will denote this as the first mechanism (O_{ex}) for PBTS instability. Noticeably, the increase of g_{Oex} during PBTS is found to decrease (partially recover) after PBTS, as shown in Fig. 3(a). Recovery of V_T due to the DOS restoration, $\Delta V_{T,DOS,rec}$, which is denoted by ③ in Fig. 4(a), can also be derived similarly to Eq. (3), by performing DOS integration as:

$$\Delta V_{T,DOS,rec}(t_{str}) = \frac{qt_{IGZO}}{C_{ox}}\left(\int_{E_V}^{E_F} g_{Oex}(E,\ t=t_{str})\,dE - \int_{E_V}^{E_F} g_{Oex}(E,\ t=t_{rec})\,dE\right). \quad (4)$$

Hence, a part of the fast recovery ($\Delta V_{T,fast}$: ② in Fig. 4(a)) should come from $\Delta V_{T,DOS,rec}$ (③ in Fig. 4(a)). By excluding the $\Delta V_{T,DOS,rec}$ from $\Delta V_{T,fast}(t_{str})$, we can determine the fast recovery component caused solely by the GI as $\Delta V_{T,shallow}(t_{str})$ (④ in Fig. 4(a)). For now, we will attribute this self-recoverable GI component as electrons de-trapping from "shallow traps" in the GI, since the electrons are able to escape the energy barrier by mere kT energy, hence the subscript. After disclosure of these two mechanisms, we are left with the remaining ΔV_T amount that does not recover in the absence of additional thermal energy, and does not originate from the DOS change in the active region. The remaining ΔV_T portion is most likely to relate with deep (in space or in energy) GI trapping, which does not recover at moderate temperatures. Hence, we will assign the last component as "deep GI trapping" (⑤ in Fig. 4(a)), which is obtained by:

$$\Delta V_{T,deep}(t) = \Delta V_{T,tot}(t) - \Delta V_{T,DOS}(t) - \Delta V_{T,shallow}(t)\ . \quad (5)$$

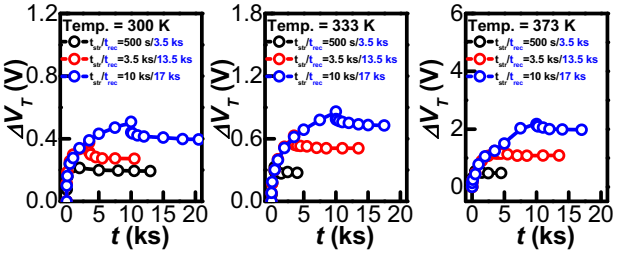

Figure 5. Measured stress-time-divided $\Delta V_T(t_{str})$ at T=300, 333, and 373 K.

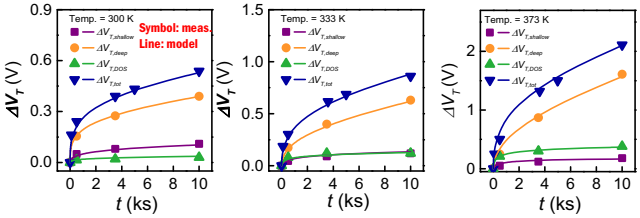

Figure 6. Decomposed $\Delta V_T(t_{str})$ at T=300, 333, and 373 K. Symbol: experiment. Line: stretched exponential model.

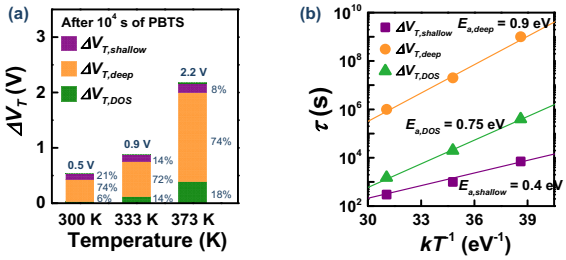

Figure 7. (a) The result of decomposing PBTS $\Delta V_{T,tot}$ into three components after $t_{str}=10^4$ s. (b) Characteristic time constant as a function of PBTS temperature to extract the effective energy barrier, i.e., activation energy E_a, for each degradation mechanism.

The three different ΔV_T portions due to PBTS are separated into three different contributions, by explicitly measuring the ΔV_T increase and recovery solely by the peroxide mechanism via DOS analysis, and by assigning the remaining fast and slow recovering portions to the shallow and deep GI trapping mechanisms, respectively [Fig. 4(c)]. The ΔV_T separations based on the stress-time-divided measurements are performed for three different stress times: t_{str1}, t_{str2}, and t_{str3}=500, 3600, and 10^4 s [Fig. 5]. Experimentally decomposed $\Delta V_{T,DOS}$, $\Delta V_{T,shallow}$, and $\Delta V_{T,deep}$ are plotted as a function of the stress time, as denoted by the symbols in Fig. 6. Figure 7(a) shows the contribution percentage of each component to the PBTS $\Delta V_{T,tot}$ after $t_{str}=10^4$ s at varying temperatures of 27, 60, 100 °C. The $\Delta V_{T,deep}$ percentage~70 % is reasonable because in this work, process conditions were controlled to minimize excess oxygen content in the GI/channel interface to reduce both $\Delta V_{T,DOS}$ and $\Delta V_{T,shallow}$, leaving the GI deep trapping component as the dominant PBTS degradation mechanism.

4. MSE Function Model

We assume the $\Delta V_{T,tot}$ under PBTS and/or recovery ($\Delta V_{T,tot}(t)=V_T(t)-V_T(t=0)$) is a combination of several components with different nature ($\Delta V_{T,tot}=\Delta V_{T1}+\Delta V_{T2}+\ldots$), and will be broken down by using experimental techniques. The time evolution of ΔV_T under bias-stress is commonly modeled by the stretched-exponential (SE) function, which is expressed as:[8,17]

$$\Delta V_{T,tot}(t) = \Delta V_{T0}\left[1-\exp\left(-\left(\frac{t}{\tau}\right)^{\beta}\right)\right] \quad (6)$$

where ΔV_{T0} is the ΔV_T at infinite time, τ is the characteristic time constant, and β is the stretching exponent with a value smaller than 1. After ΔV_T decomposition from PBTS at various temperatures, each degradation mechanism component will possess its own set of fitting parameters to the SE function (ΔV_{T0}, $\tau=\tau_0\times\exp(E_a/kT)$, β, and E_a). Therefore, $\Delta V_{T,tot}(t)$ can be modeled by using the MSE function as:

$$\Delta V_{T,tot}(t) = \Delta V_{T,DOS}(t)+\Delta V_{T,deep}(t)+\Delta V_{T,shallow}(t) \quad (7)$$
$$= \Delta V_{T0,DOS}\left[1-\exp\left(-\left(\frac{t}{\tau_{DOS}}\right)^{\beta_{DOS}}\right)\right]+\Delta V_{T0,deep}\left[1-\exp\left(-\left(\frac{t}{\tau_{deep}}\right)^{\beta_{deep}}\right)\right]$$
$$+\Delta V_{T0,shallow}\left[1-\exp\left(-\left(\frac{t}{\tau_{shallow}}\right)^{\beta_{shallow}}\right)\right]$$

The lines in Fig. 6 show that all of $\Delta V_{T,DOS}$, $\Delta V_{T,shallow}$, and $\Delta V_{T,deep}$ are well fitted with the SE functions with individual parameters and the $\Delta V_{T,tot}(t)$ is well described by the superposition of MSE functions. It suggests the assumption in Eq. (7) is reasonable. The effective energy barrier E_a is found to be 0.75, 0.40, 0.90 eV for the ΔV_T due to DOS increase, GI shallow trapping, and GI deep trapping, respectively, by using the temperature-dependence of τ, as shown in Fig. 7(b). Effective energy barrier values $E_{a,shallow}$= 0.40 eV and $E_{a,deep}$= 0.90 eV is in good agreement with values from studies where charge trapping was the dominant mechanism, where E_a values range from 0.38 to 1.33 eV.[17,18] On the other hand, it is noteworthy that the extracted $E_{a,DOS}$= 0.75 eV coincides with the energy difference between the calculated oxygen interstitial (O_i) level and the Fermi-level under PBTS.[15] Considering the activation energy for the peroxide dissociation through electron trapping has been calculated to be 0.8-0.9 eV,[15,16] the extracted $E_{a,DOS}$= 0.75 eV is well within range of previously reported values lending confidence to the proposed method to partition the $\Delta V_{T,DOS}$ component.

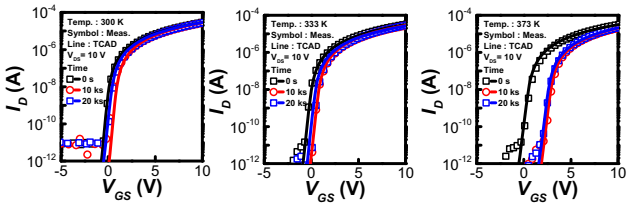

Figure 8. The TCAD-simulated I-V curves (line) compared with measured ones (symbol).

5. TCAD Simulation-Based Verification

In order to validate the decomposed PBTS degradation mechanisms, the PBTS time-evolution of DOS is incorporated into TCAD simulation tool[19], which quantitatively reflects the $\Delta V_{T,DOS}$ components. The electron trapping into GI shallow/deep traps is also taken into account by tuning the electron trapping-related TCAD model parameters, such as the energy level, band offset, spatial position/density, capture cross section, and escape frequency of GI shallow/deep traps. Figure 8 shows that our TCAD simulation results reproduce the measured PBTS time-evolutions of I-V curves very well. It suggests the validities of our decomposition method and the proposed instability mechanisms.

6. Conclusions

We have demonstrated a universal method to experimentally determine the quantitative contributions of PBTS instability mechanisms in the TG SA coplanar a-IGZO TFTs by combining the stress-time-divided measurements and the DOS extraction. We have successfully decomposed the ΔV_T caused by PBTS into three mechanisms: 1) increase of DOS due to excess oxygen in the active region, 2) shallow and 3) deep charge trapping in the GI components. The MSE model is used to obtain a separate set of fitting parameters for each experimentally determined component and to gain insight into the physical origin of PBTS instability. We validated the proposed method by comparing the TCAD simulation results with the measured data. Our results can be easily applied universally to any device with any stress conditions, along with guidelines for process optimization efforts towards ultimate PBTS stability.

7. Acknowledgements

This work was supported by the National Research Foundation of Korea (NRF) funded by the Korean Government (MSIP) under Grant 2016R1A5A1012966 and 2015M3D1A1068061. The TCAD software was supported by IC Design Education Center (IDEC).

8. References

[1] R. Tani et al., SID Digest 46, 950 (2015).

[2] Z. Wu et al., SID Digest 46, 954 (2015).

[3] B. Yeh and C. Lin, SID Digest 46, 943 (2015).

[4] C. Ha et al., SID Digest 46, 1020 (2015).

[5] M. E. Lopes et al., Appl. Phys. Lett. 95, 063502 (2009).

[6] S. Oh et al., Appl. Phys. Lett. 108, 141604 (2016).

[7] A. Janotti and C. G. Van de Walle, Phys. Rev. B. 76, 165202 (2007).

[8] A. J. Flewitt and M. J. Powell, J. Appl. Phys. 115, 134501 (2014).

[9] H.-H. Nahm and Y.-S.Kim, NPG Asia Mat. 6, e143 (2014).

[10] M.J. Powell, IEEE Trans. Electron Device 36, 2753 (1989).

[11] J. U. Bae et al., SID Digest 44, 89 (2013).

[12] S. Oh et al., IEEE Electron Device Lett. 35, 1037 (2014).

[13] S. Choi et al., IEEE Electron Device Lett., accepted (2017).

[14] H. Bae et al., IEEE Electron Device Lett. 34, 1524 (2013).

[15] W. H. Han et al., Phys. Rev. App. 3, 044008 (2015).

[16] H.-H. Nahm, Y.-S. Kim, and D. H. Kim, Phys. Status Solidi B 249, 1277 (2012).

[17] T. Chen et al., Appl. Phys. Lett. 97, 112104 (2010).

[18] C. Han et al., Jpn. J. Appl. Phys. 53, 08NG04 (2014).

[19] ATLAS Device Simulation Software User's Manual (Silvaco, Santa Clara, CA, 2005).